Panovska, S., Constable, C. G., Korte, M. (2018): Extending global continuous geomagnetic field reconstructions on timescales beyond human civilization. - *Geochemistry Geophysics Geosystems (G3)*, *19*, 12, pp. 4757—4772.

DOI: http://doi.org/10.1029/2018GC007966

AGU100 ADVANCING EARTH AND SPACE SCIENCE

Geochemistry, Geophysics, Geosystems

RESEARCH ARTICLE
10.1029/2018GC007966

**Key Points:**
- The first, global, time-dependent geomagnetic field model covering the past 100 ka is presented
- Smoothing kernels are used in the forward modeling to account for different temporal resolutions in paleomagnetic sediment records
- Geomagnetic excursions, dipole moment variations, the time-averaged field, and PSV activity over the past 100 ka are discussed

**Supporting Information:**
- Supporting Information S1
- Data Set S1

**Correspondence to:**
S. Panovska,
panovskasanja@yahoo.com

**Citation:**
Panovska, S., Constable, C. G., & Korte, M. (2018). Extending global continuous geomagnetic field reconstructions on timescales beyond human civilization. *Geochemistry, Geophysics, Geosystems*, *19*, 4757–4772. https://doi.org/10.1029/2018GC007966

Received 14 SEP 2018
Accepted 7 DEC 2018
Accepted article online 12 DEC 2018
Published online 28 DEC 2018



# Extending Global Continuous Geomagnetic Field Reconstructions on Timescales Beyond Human Civilization

**S. Panovska[1,2], C. G. Constable[2], and M. Korte[1]**

[1]Helmholtz Zentrum Potsdam, Deutsches GeoForschungsZentrum GFZ, Potsdam, Germany, [2]Institute for Geophysics and Planetary Physics, Scripps Institution of Oceanography, University of California, San Diego, La Jolla, CA, USA

**Abstract** Study of the late Quaternary geomagnetic field contributes significantly to understanding the origin of millennial-scale paleomagnetic secular variations, the structure of geomagnetic excursions, and the long-term shielding by the geomagnetic field. A compilation of paleomagnetic sediment records and archeomagnetic and lava flow data covering the past 100 ka enables reconstruction of the global geomagnetic field on such long-term scales. We use regularized inversion to build the first global, time-dependent, geomagnetic field model spanning the past 100 ka, named *GGF100k* (*G*lobal *G*eomagnetic *F*ield over the past *100 k*a). Spatial parametrization of the model is in spherical harmonics and time variations with cubic splines. The model is heavily constrained by more than 100 continuous sediment records covering extended periods of time, which strongly prevail over the limited number of discrete snapshots provided by archeomagnetic and volcanic data. Following an assessment of temporal resolution in each sediment's magnetic record, we have introduced smoothing kernels into the forward modeling when assessing data misfit. This accommodates the smoothing inherent in the remanence acquisition in individual sediment paleomagnetic records, facilitating a closer fit to both high- and low-resolution records in regions where some sediments have variable temporal resolutions. The model has similar spatial resolution but less temporal complexity than current Holocene geomagnetic field models. Using the new reconstruction, we discuss dipole moment variations, the time-averaged field, and paleomagnetic secular variation activity. The new GGF100k model fills the gap in the geomagnetic power spectrum in the frequency range 100–1,000 $Ma^{-1}$.

## 1. Introduction

Paleomagnetic records provide the possibility of recovering the geomagnetic field evolution beyond the age of systematic ground and satellite measurements and of historical observations of the Earth's magnetic field. Our knowledge of the past geomagnetic field is steadily improving. There are now several global, time-varying paleomagnetic field models spanning the Holocene (e.g., Constable et al., 2016, 2015; Korte & Constable, 2003, 2005, 2011; Korte et al., 2011; Nilsson et al., 2014; Panovska et al., 2015; Pavón-Carrasco et al., 2014). On longer timescales ranging up to 2 million years, the global geomagnetic field evolution has only been studied in terms of paleointensity or dipole moment variations (e.g., Channell et al., 2009; Guyodo & Valet, 1996, 1999; Laj et al., 2004; Stoner et al., 2002; Valet et al., 2005; Ziegler et al., 2011). Capturing the temporal evolution draws heavily on sedimentary records, but time-averaged field models based on paleomagnetic data from lava flows also exist and they describe the spatial characteristics of normal and reverse polarity fields (e.g., Cromwell et al., 2018; Gubbins & Kelly, 1993; Johnson & Constable, 1995, 1997; Kelly & Gubbins, 1997).

Ground and satellite observations reveal a decay of the geomagnetic axial dipole during the last 170 years (Finlay et al., 2016), an observation confirmed by recent measurements of the global geomagnetic field by the satellite mission Swarm (Olsen et al., 2015). It has been repeatedly suggested that this weakening of the geomagnetic field may indicate an impending excursion or reversal (Gubbins, 1987; Hulot et al., 2002; Laj & Kissel, 2015; Pavón-Carrasco & De Santis, 2016). However, in general, decreases like the present one are followed by subsequent periods of recovery in field strength. A decrease in field intensity has also been seen many times in the Earth's history prior to and during geomagnetic excursions and reversals (e.g., Laj & Channell, 2015; Roberts, 2008; Singer, 2014). Extension of global spherical harmonic models of the geomagnetic field beyond the Holocene, to span the past 100 ka, includes the well-documented Laschamp (~41 ka) and Mono

Lake (~34 ka) excursions and several disputed excursions such as Hilina Pali (~17 ka; Singer et al., 2014), Rockall (~26 ka; Channell et al., 2016), Norwegian-Greenland Sea (~60 ka; Nowaczyk et al., 1994), Fram Strait (~91 ka; Worm, 1997), post-Blake (~95 ka; Thouveny et al., 2004), or Skálamælifell excursion (~91 ka; Jicha et al., 2011). Although efforts have been made in the past to model the transitional field during geomagnetic excursions (for instance, models of the Laschamp excursion, the IMOLE, Leonhardt et al., 2009, and LSMOD.1, Brown et al., 2018), these have not yet been placed in the broader context of the field evolution up to recent times. Moreover, modeling the field on multimillennial timescales will provide the basis for studying the temporal variability of geomagnetic shielding and its effects on cosmogenic isotope production. For example, a peak of Chlorine-36 data from the Greenland Ice Core Project is linked to a period of low geomagnetic field intensity (Baumgartner et al., 1998).

In this paper, we use a comprehensive data set recently compiled by Panovska et al. (2018) and summarized in section 2 to reconstruct the evolution of the geomagnetic field over the past 100 ka. The basic inverse modeling strategy used for the HFMx Holocene models (Panovska et al., 2015) is employed here (section 3) with modifications to enable accounting for variable temporal resolution in the paleomagnetic sediment records. This is done by introducing unique temporal smoothing kernels appropriate for each sediment record into the forward model, enabling a better fit to both high- and low-resolution records (section 3.1). The modeling results are discussed in section 4 in terms of fit to the data, dipole moment variation, time-averaged field, and power spectral density.

## 2. Data

The data compilation used to build the model has been described in detail in Panovska et al. (2018). It consists of paleomagnetic data from marine sediments, a few lacustrine sediments covering mostly the Holocene, and volcanic and archeomagnetic data. The sediment data were compiled from various sources including the SEDPI06 collection (Tauxe & Yamazaki, 2007), the MagIC database at https://Earthref.org/MagIC (Constable et al., 2006; Jarboe et al., 2012), the sediment part of GEOMAGIA50.v3 (Brown, Donadini, Nilsson, et al., 2015), Pangaea (Diepenbroek et al., 2002), records longer than 10 ka from the Holocene compilation of Korte et al. (2011), and newly published sediment records provided directly by individual authors. The average length of the sediment records, counting each of the three components separately, is 62 ka, with a minimum length of 3 ka and a maximum of 100 ka. The individual records contain vastly different numbers of data (the average is 541), with a mean of 14 data points per thousand years (see supporting information Figure S1). Volcanic and archeomagnetic data were drawn from the GEOMAGIA50 database (Brown, Donadini, Korte, et al., 2015; Korhonen et al., 2008) for the period 0 to 50 ka and the subset of the global 0- to 10-Ma PSV10 data set (Cromwell et al., 2018) covering 50 to 100 ka. We used 14,505 archeomagnetic and volcanic data in total, all with absolute age constraints. However, their distribution is strongly biased toward more recent epochs; thus, 74.6% and 90.4% of these data cover the past 3 and 10 ka, respectively. Although the absolute volcanic data are very sparse in the 10- to 100-ka period, they play a key role in the calibration of relative paleointensity (RPI) and relative declination from the sediment records. Spatial and temporal distributions of the data are presented in Figures 1a and 1b, respectively. The number of sediment data is continually increasing toward the present time, with a noticeable bump over the Laschamp excursion and significantly higher number of directional data compared to RPI for the Holocene period. Figure 1c gives an indication of the sampling at the core-mantle boundary (CMB) over the whole 100 ka interval in the form of the combined linearized data kernel, summed up for all data types and components (for equations see Johnson & Constable, 1997). The model is best constrained by data in northern midlatitudes in the Atlantic Ocean, while moderately constrained areas appear over South America and midlatitudes to equatorial latitudes in the Pacific Ocean. The Indian and Southern Oceans are poorly sampled, and future drillings are needed in these regions to improve the model reliability.

A variety of dating methods have been used to assign age scales to sediment magnetic records including radiocarbon, oxygen isotopes, correlations based on physical or magnetic properties, varves, tephras, pollen, and combinations of methods for improving the age-depth models. For the purpose of modeling, we have selected a portion of the whole data compilation, here called semidependent data set, that was also used by Panovska et al. (2018) to analyze PSV activity over the past 100 ka. This data set contains all paleomagnetic sediment records whose timescales are dated independently of correlations made via RPI variations or PSV, together with sediment records whose independent age models have been complemented with tie points

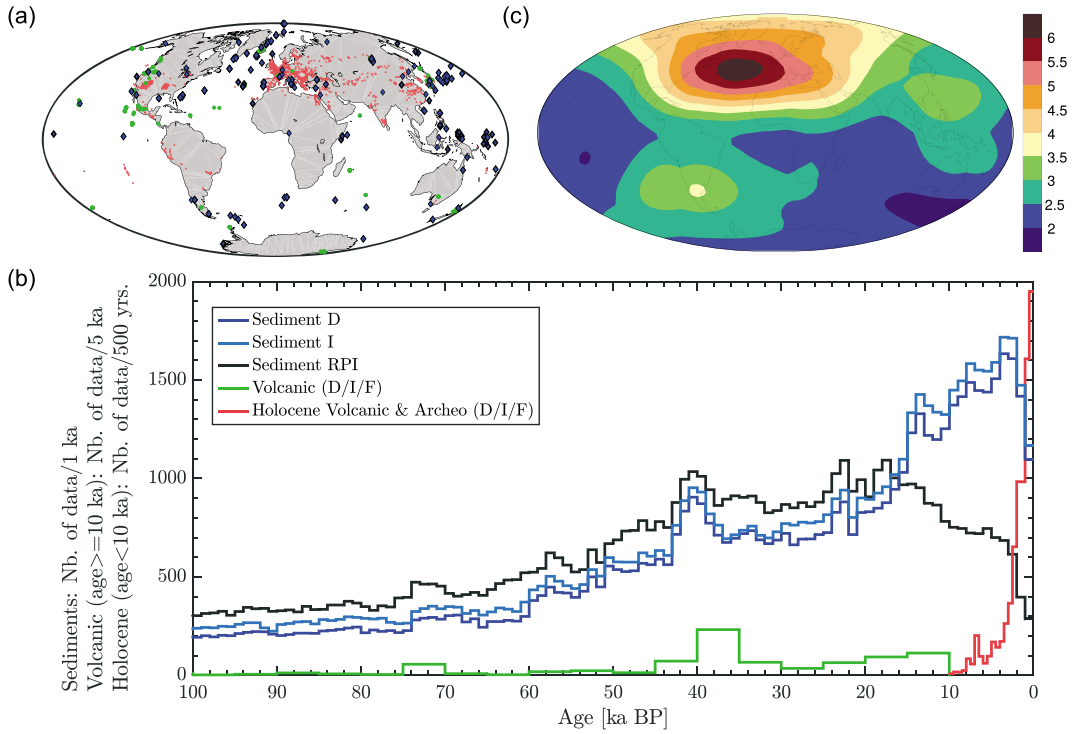


**Figure 1.** (a) The global spatial distribution of the paleomagnetic sediment records (blue diamonds) and volcanic and archeomagnetic data covering the past 120 ka (with green dots for data older than 10 ka and Holocene data with red dots). (b) Temporal distributions of declination, inclination, and RPI of sediment magnetic records, and archeomagnetic and volcanic data with the three components presented together because of the small number of data. Different width binning is used in order to present the temporal data distribution on one plot; note the *y* axis label. (c) Sum of data kernels indicating sampling of the core-mantle boundary by all components and all data types; sediment, volcanic, and archeomagnetic data from the semidependent data set are used to build the GGF100k model. RPI = relative paleointensity.

that in most cases are related to the occurrence of geomagnetic excursions. In total, there are 97 relative declination, 110 inclination, and 135 RPI sediment records.

We used the method described by Panovska et al. (2012) to estimate the random variability present in each of the sediment records compiled in Panovska et al. (2018). This provides uncertainty estimates for the data via an assessment of the residuals after fitting a penalized least squares cubic spline. The estimates obtained in this way exhibit a rather large range of values indicating the variable quality of the sediment records. Median values and interquartile ranges for individual components are 15.2° (8.4° to 31.2°) for declination, 5.8° (3.2° to 8.2°) for inclination, and 4.7 μT (3.0 to 7.9 μT) in absolute units for RPI. Calibration of RPI uncertainties to absolute values was carried out using a spline fit to volcanic and archeomagnetic data covering the past 100 ka, as discussed by Panovska et al. (2018). An important aspect of the uncertainty estimation technique is that it also provides a measure of temporal resolution for each sediment record: these range from several decades to more than 10,000 years necessitating an accommodation of this variability in our forward modeling strategy, as described in more detail in section 3.1. Systematically different regional sedimentation rates and data densities might influence the resulting model resolution. Smoothing time and sedimentation rate variations as a function of latitude and longitude (supporting information Figure S2) show that although some Pacific hemisphere records have lower sedimentation rates and consequently higher smoothing times, a sufficient number of high-resolution records from all over the globe exist to preclude biases in resulting model resolution.

In some cases, where the uncertainty analysis yielded unrealistically small estimates (e.g., inherently smoothed measurements made in pass-through magnetometers), it is important to ensure that these records are not given too much weight in the model. Therefore, we introduced minimum uncertainties expressed in terms of the $\alpha_{95}$ confidence circle for directions and in microtesla for intensity. The minimum threshold values are $\alpha_{95}$ of 6° for directions and 5 μT for the intensity, as previously used in the Holocene CALS models (Korte

et al., 2009; Korte & Constable, 2011). Twenty-two percent of declination and 29% of inclination sediment records and almost half of the RPI records were assigned minimum uncertainties. Minimum uncertainties were assigned to archeomagnetic and volcanic data with either missing or unrealistically small uncertainties, in the form of $\alpha_{95}$ of 4.3° for directions and 5 μT for intensity data. Equations for converting $\alpha_{95}$ to standard deviations of declination and inclination can be found in Donadini et al. (2009).

## 3. Modeling Method

The basic methodology employed to build the GGF100k model has been used before for a range of global, time-dependent models based on paleomagnetic and archeomagnetic data spanning the Holocene (e.g., Constable et al., 2016; Korte & Constable, 2005; Korte et al., 2011; Panovska et al., 2015). Spherical harmonics up to degree and order 10 in space provide the spatial basis functions of the model. A cubic B-spline basis is adopted for the temporal evolution of the Gauss coefficients with a knot spacing of 200 years. In total, 606 knot points cover the interval from 0 to 120 ka BP, but the model is considered valid only for the past 100 ka in order to avoid undesirable end effects.

The usual modeling strategy, as outlined, for example, in Korte and Constable (2003), predicts a magnetic field observation based on the vector derivative of a Laplacian potential $V$ described by a spherical harmonic field model with time-varying coefficients $g_l^m(t)$ and $h_l^m(t)$ as given in the following equations.

$$V(r,\theta,\phi,t) = R_E \sum_{l=1}^{l_{\max}} \sum_{m=0}^{l} \sum_{n=1}^{n_{\max}} \left(\frac{R_E}{r}\right)^{l+1} [g_l^{m,n}\cos(m\phi) + h_l^{m,n}\sin(m\phi)] P_l^m(\cos\theta) M_n(t) \quad (1)$$

where $(r,\theta,\phi)$ representing radius, colatitude, and longitude, are spherical polar coordinates and $R_E$ = 6,371.2 km is the mean radius of the Earth's surface. The $P_l^m(\cos\theta)$ are the Schmidt quasi-normalized associated Legendre functions of degree $l$ and order $m$. The time variation in Gauss coefficients is described by cubic B-splines:

$$g_l^m(t) = \sum_{n=1}^{n_{\max}} g_l^{m,n} M_n(t) \quad (2)$$

and the same for $h_l^m$. Cubic B-splines are piecewise cubic polynomials, which form a basis of minimal support De Boor (2001). The $i$th cubic B-spline is nonzero ($M_i(t) > 0$) only if $t$ lies in the interval $[t_i, t_{i+4}]$ of knot points $t_n$, $n = 1$ to $n_{\max}$. A new feature in our modeling strategy is to accept that variable temporal resolution in the data drawn from sediment records used in creating the model must be accommodated in the forward modeling procedure. This is accomplished by using a suitable smoothing kernel or temporal filter to modify the model prediction and more accurately estimate what we expect for each sediment record at any given time and location.

### 3.1. Forward Modeling With a Smoothing Kernel

As already noted the penalized spline fits to individual records applied for obtaining uncertainty estimates (Panovska et al., 2018) provide an assessment of the temporal resolution in each sediment record (e.g., Constable & Parker, 1988; Korte & Constable, 2008). One of the output parameters of the uncertainty analysis is the inherent smoothing time for each paleomagnetic record that denotes the timescale it can resolve (for examples of Holocene records, see Panovska et al., 2012). This is acquired in the following way. A delta function is inverted at each internal data point of the record with the same smoothing parameter as for the smoothing spline fit (e.g., Parker, 1994) to produce the resolving kernel. This temporal resolving kernel is described by the full width at half maximum (FWHM) for each point, and averaged values ($T_{ss}$) are estimated for each paleomagnetic sediment record. For the analysis of all sediment records in the 100-ka compilation, smoothing times range from 40 years to about 13.8 ka with a median of 400 years (Panovska et al., 2018). Smoothing inherent in the sediment record is approximated by convolution of each model prediction with a Gaussian kernel with appropriate temporal resolution specified by its standard deviation.

The smoothing time $T_{ss}$ (i.e., FWHM) is converted to the appropriate standard deviation which specifies the width for the kernel. The relationship between the standard deviation and $T_{ss}$ can be found with the probability density function for the Gaussian distribution with mean $\mu$ and standard deviation $\sigma$:

$$P(t,\mu,\sigma^2) = \frac{1}{\sigma\sqrt{2\pi}} \exp\left[-\frac{(t-\mu)^2}{2\sigma^2}\right] \quad (3)$$

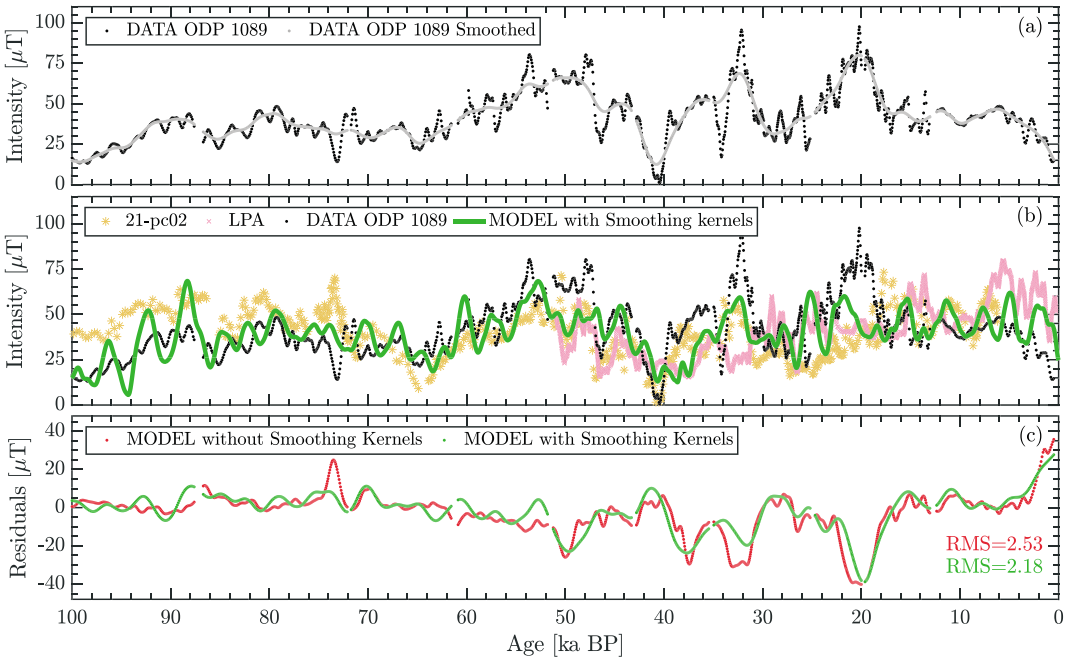


**Figure 2.** Testing the implementation of smoothing kernel at the location of ODP 1089. (a) The three components of ODP 1089 are smoothed with $T_{ss}$ = 1,000 years, and the smoothed records are used to build a model with and without smoothing kernels. (b) Predictions at the ODP 1089 location are compared with intensity data from nearby locations (21-pc02, South Atlantic, Stoner et al., 2002, 2003; and LPA, Laguna Potrok Aike in Argentina, Lisé-Pronovost et al., 2013) to check their influence on the model with implemented smoothing kernels. (c) Comparison of residuals of the two models to the smoothed ODP 1089 data (gray dots in subplot a) used to constrain the models; that is, predictions of the model with smoothing kernels are smoothed with $T_{ss}$ = 1,000 years, and individual epoch predictions are used for the model without smoothing kernels. RMS normalized misfits are given in corresponding colors. ODP = Ocean Drilling Program; RMS = root-mean-square.

If the mean is 0, the FWHM is the distance between the points $-t_{\text{fwhm}}$ and $+t_{\text{fwhm}}$, which correspond to half maximum value. For a normal distribution, the mean corresponds to the peak or mode, and $t_{\text{fwhm}}$ can be found from $P(t_{\text{fwhm}}) = P(\mu)/2$:

$$\frac{1}{\sigma\sqrt{2\pi}}\exp\left(-\frac{t_{\text{fwhm}}^2}{2\sigma^2}\right) = \frac{1}{2}\frac{1}{\sigma\sqrt{2\pi}} \tag{4}$$

For $\sigma \neq 0$, $t_{\text{fwhm}} = \pm\sqrt{2\sigma^2 \ln 2}$. From this it follows that

$$T_{ss} = 2t_{\text{fwhm}} = 2\sqrt{2\sigma^2 \ln 2} = \sigma\sqrt{8 \ln 2} = 2.3548\sigma \tag{5}$$

Once $T_{ss}$ is converted to standard deviation, the Gaussian kernel is defined as

$$K(t, t_i) = \exp\left(\frac{\|t - t_i\|^2}{2\sigma^2}\right) \tag{6}$$

For convolution purposes, the size of the kernel is taken to be $\pm 3\sigma$ and is approximated to 0 elsewhere. The kernel is applied to each data point with $T_{ss}$ larger than the spline knot spacing used for the time representation of the model (here 200 years). For a given kernel $K(t, t_i)$, the weight sequence is defined by

$$w_i(t) = \frac{K(t, t_i)}{\sum_{i=1}^{i_{\max}} K(t, t_i)} \tag{7}$$

where $\sum_{i=1}^{i_{\max}} w_i(t_i) = 1$. If no smoothing is needed, the misfit between the observations ($d$) and the raw model predictions is $d_i - f(m)_i$, with $f(m)$ expressing the model prediction, whereas with the smoothing kernel the more realistic misfit is estimated from $d_i - \hat{f}(m)_i$ where

$$\hat{f}(m)_i = \sum_{i=1}^{i_{\max}} w_i(t) f(m)_i \tag{8}$$

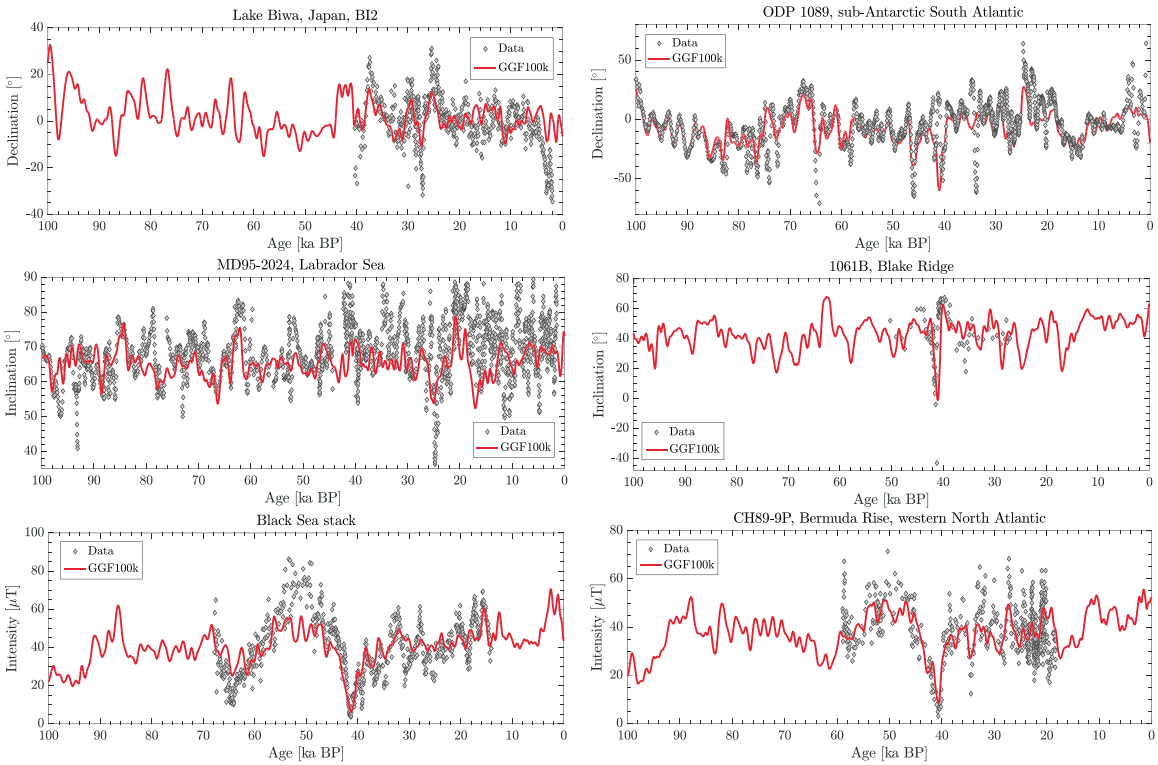


**Figure 3.** Model predictions for six sediment paleomagnetic records and different field components compared to the sediment data. Sediment records: BI2, Lake Biwa, Japan (Hayashida et al., 2007); ODP 1089, sub-Antarctic South Atlantic (Stoner et al., 2003); MD95-2024, Labrador Sea, Atlantic (Stoner et al., 2000); 1061B, Blake Ridge, Atlantic (Bourne et al., 2013); Black Sea (Nowaczyk et al., 2013); and CH89-9P, North Atlantic (Lund et al., 2005). Relative paleointensity data were calibrated using the scaling factors obtained from the GGF100k model. All records are plotted for the 0- to 100-ka time period. ODP = Ocean Drilling Program.

Figure 2a shows a simulated example of the effect of the smoothing kernel on the prediction of paleomagnetic observations. Paleointensity data from Ocean Drilling Program (ODP) 1089 (black dots) from the South Atlantic Ocean (Stoner et al., 2003) are smoothed with $T_{ss}$=1,000 years to simulate a lower-resolution sedimentary record with data samples given by the gray dots. Details of the modeling are described in section 3.2, but here we illustrate the general impact to be expected from our improved forward modeling. In Figure 2b predictions of the model with smoothing kernels are compared with sediment records from nearby locations to illustrate their effect on the model. The model captures not only some high-frequency variations present in the raw ODP 1089 record but also variations from nearby locations, for instance, 21-pc02 record (Channell et al., 2000; Stoner et al., 2002), and the very detailed LPA sediment record (Lisé-Pronovost et al., 2013) with estimated $T_{ss}$ of 110 years has pronounced effects over its whole duration of 0–50 ka. In Figure 2c we show how a model that does not take account of the smoothing in the forward model in all three components has generally larger residuals than one that does.

### 3.2. Inversion to Find a Model

Using the adaptive forward problem described above, we find the usual solution for a time-varying geomagnetic field model by minimization of an objective functional that contains the $L_2$ measure of misfit to the data $Q(\mathbf{m})$ and a measure of model complexity (e.g., Gubbins & Bloxham, 1985):

$$Q(\mathbf{m}) + \lambda_S \Psi(\mathbf{m}) + \lambda_T \Phi(\mathbf{m}) \tag{9}$$

The damping parameters, $\lambda_S$ and $\lambda_T$, that describe the trade-off between the misfit and the model spatial and temporal norms ($\Psi$ and $\Phi$) were chosen with trade-off curves (supporting information Figure S3). We have chosen the Ohmic heating (dissipation) norm (Bloxham & Jackson, 1992; Gubbins & Bloxham, 1985; Korte et al., 2011) and a norm based on the second time derivative of the radial magnetic field integrated over the CMB (Bloxham & Jackson, 1992; Jackson et al., 2000; Korte & Constable, 2005) for regularization in space and time, respectively. We used declination and intensity in relative form and estimated the calibration coefficients and

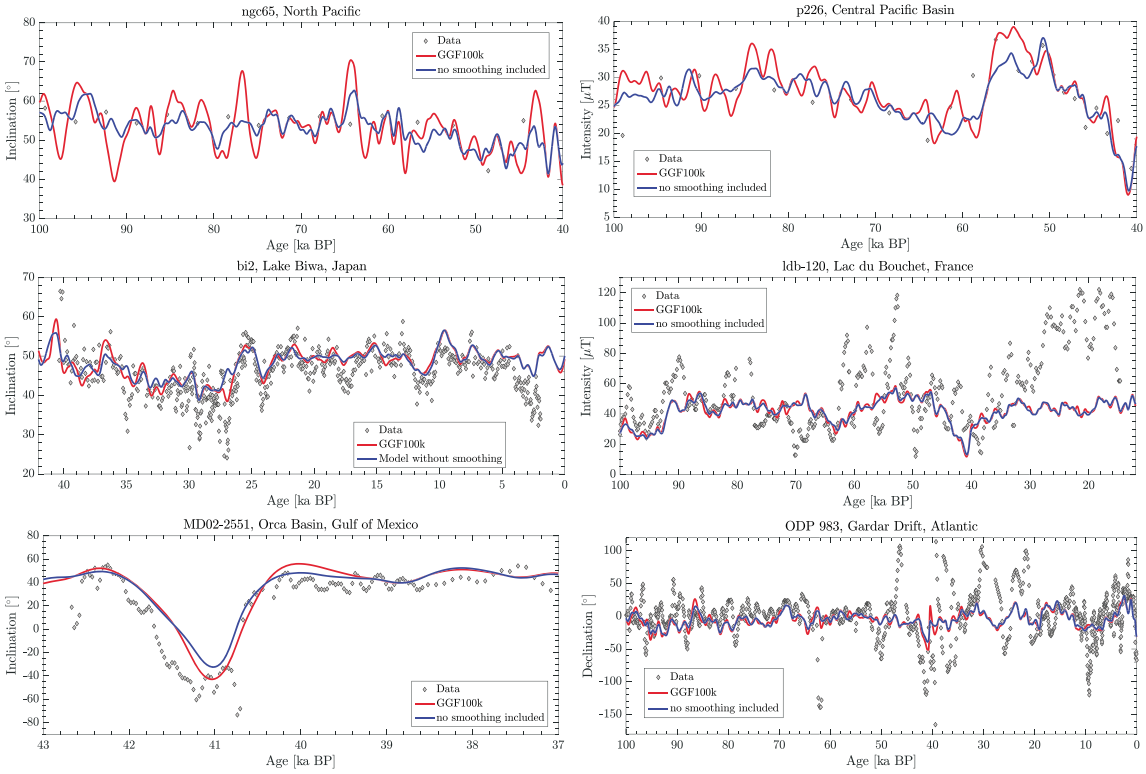


**Figure 4.** Comparison between some examples of predictions from the model GGF100k and a model with no smoothing kernels included in the forward modeling. Sediment records: ngc65, North Pacific (Yamazaki, 1999); p226, Central Pacific (Yamazaki et al., 1995); bi2, Lake Biwa, Japan (Hayashida et al., 2007); ldb-120, Lac du Bouchet (Thouveny et al., 1990); MD02-2552, Orca Basin, Gulf of Mexico (Laj et al., 2006); and ODP 983, Gardar Drift, North Atlantic (Channell et al., 1997; Channell, 1999). Relxative paleointensity data were calibrated using the scaling factors obtained from the GGF100k model. Note the different time intervals covered by the records for clarity of the differences between the two curves and fits to the data. ODP = Ocean Drilling Program.

scaling factors within the inversion using the method described in Panovska et al. (2015). A constant axial dipole term $g_1^0 = -30\mu T$ for the entire time span is used as a starting model for the Gauss coefficients; initial calibration coefficients for RPI were estimated by comparison to a spline fit through the archeomagnetic and volcanic data over the past 100 ka, and initial scalings for declination records were set to 0 (zero-mean declination records are input data to the model). The adjustment of calibration coefficients is highest in the first few iterations, and they stabilize after four iterations (see supporting information Figure S4 for declination and Figure S5 for RPI calibration factors, and the final values after 10 iterations in Figures S6 and S7, respectively). Declination data that showed transitional behavior defined by the PSV index being larger than 0.5 (Panovska & Constable, 2017) are excluded from the calibration process for declination. The inversion is performed using iterative data rejection at the level of 3 standard deviations in the residuals (10% of the data were rejected in the final model). We have also tested an iterative data rejection at 5 standard deviations, which resulted in 3% of the data being rejected. Similar levels of the spatial and temporal norms were achieved, but the misfit is higher when more data are included. In the model with rejection at 3 standard deviations better convergence of the spatial norm changes is achieved as well as better fit to the data especially over the Laschamp excursion (see supporting information Figure S8 for example predictions). The temporal distribution of rejected data shows that the largest fraction of data are rejected around the Laschamp excursion and during the most recent ~5 ka (supporting information Figure S9). Rejected intensity data are fairly uniformly distributed over the whole time span, whereas directional data rejection peaks during the Laschamp excursion, probably as a consequence of inconsistent ages during large and rapid directional variations.

In Figure 3 we present some examples of the GGF100k model predictions of inclination, declination, and intensity for globally distributed sediment records. The effects of implementing the smoothing kernels are presented for a range of geographic locations in Figure 4. Here the GGF100k model predictions are compared with a model built with the same data set and damping parameters as the GGF100k but no smoothing kernels applied. Significant differences are observed in the Pacific region, which is characterized by sediment

**Table 1**
*Damping Parameters, Misfits, and Number of Data for the GGF100k Model*

| Quantity | Value |
|---|---|
| Spatial | |
| Parameter $\lambda_S$ [nT$^{-2}$] | $1.8 \times 10^{-14}$ |
| Norm $\Psi$ [nT$^2$] | $1.8 \times 10^{13}$ |
| Temporal | |
| Parameter $\lambda_T$ [nT$^{-2}$year$^4$] | $3.6 \times 10^{-2}$ |
| Norm $\Phi$ [nT$^2$ year$^{-4}$] | 2.48 |
| RMS[a] | |
| Global | 1.15 |
| Sediment | 1.14 |
| Volcanic | 1.25 |
| Declination | 1.00 |
| Inclination | 1.16 |
| Intensity | 1.27 |
| Number of data | |
| Total | 199.377 |
| Final model | 179.356 |

[a]The RMS misfit is normalized by the data uncertainty estimates. RMS = root-mean-square.

paleomagnetic records with low sedimentation rates. The inversion with kernel smoothing produces greater temporal variability at locations of the sediment records ngc65, North Pacific (Yamazaki, 1999) and p226, central Pacific (Yamazaki et al., 1995) as a result of better fitting to nearby higher-resolution records. Model predictions in other regions (Atlantic Ocean and Europe) are relatively unaffected and show only minor differences.

## 4. Results and Discussion

### 4.1. Resolution and Energy Spectrum of the Model

Model parameters, norms, and root-mean-square misfits of the presented model GGF100k are given in Table 1. The final misfit of the model normalized with the data uncertainty estimates is 1.15. Root-mean-square misfit estimates separately for each component and data type show the best fit for declination, which is a result of the large uncertainty estimates of declination, and better fit to the sediments compared to volcanic and archeomagnetic data.

Spatial power spectra for the time-averaged main field and secular variation at the CMB are plotted in Figure 5. For comparison we have added the spectra of the high-resolution model *gufm-sat-E3* over the decade 2000–2010 (Finlay et al., 2012) and the Holocene field models CALS10k.2 and HFM.OL1.A1 (both averaged over the past 10 ka; Constable et al., 2016). In general, the GGF100k model shows similar spatial structure to CALS10k.2 (up to degree 5) but higher power at degrees 3 to 10 compared to HFM.OL1.A1. Temporally, as expected, the GGF100k model has the lowest power for all degrees, with a similar trend to the HFM.OL1.A1 model, indicating the limited resolution of global models on longer timescales. The model with smoothing kernels shows comparable spatial but higher temporal variability for degrees 1 to 3.

Time evolution of the individual dipole and quadrupole Gauss coefficients of the GGF100k model are presented in supporting information Figures S10 and S11. The Laschamp excursion at 41 ka is clearly seen as a minimum in absolute value of the axial dipole coefficient (i.e., maximum in the figure), but neither of the equatorial dipole or higher-degree coefficients shows any special signature during that time. For reference, we have compared the dipole and quadrupole coefficients for the Holocene period with the models CALS10k.1b (Korte et al., 2011), CALS10k.2 and HFM.OL1.A1 (Constable et al., 2016), and pfm9k.1a (Nilsson et al., 2014) in supporting information Figures S12 and S13. There is a good general agreement for most of the coefficients, except for a systematic offset observed between the GGF100k and the Holocene models in the $g_2^0$ coefficient for most of the Holocene period. These differences may arise in part from the fact that in the GGF100k model

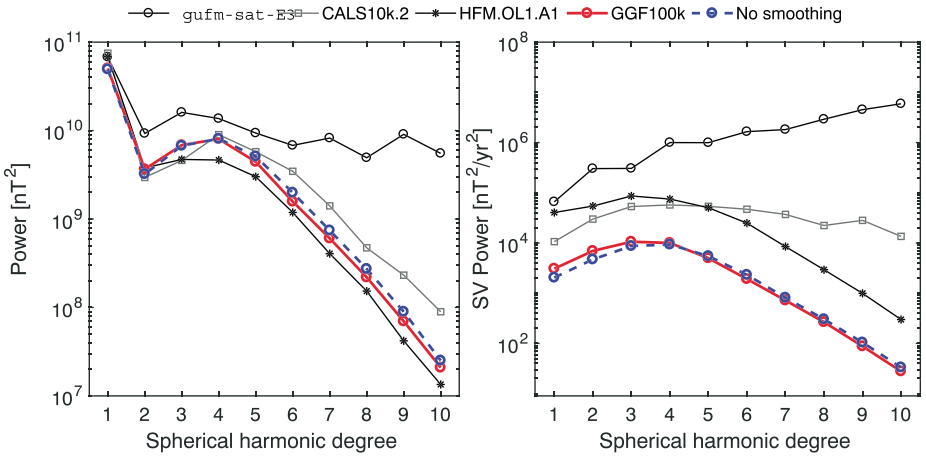


**Figure 5.** Comparison of the spherical harmonic spectra of the time-averaged geomagnetic field and its secular variation at the core-mantle boundary. Spectra of the model *gufm-sat-E3* ($L = 24$) is plotted only to degree 10 for comparison purposes. Models: *gufm-sat-E3* (Finlay et al., 2012); CALS10k.2 and HFM.OL1.A1 (Constable et al., 2016); GGF100k; and a 100-ka model without smoothing kernels.

we used only one third of the data that constrain the Holocene models, namely, those records that extended beyond 10 ka in age. Additional sediment records that were not used in the CALS10k.2 and HFM.OL1.A1 models have been employed in GGF100k. They mostly come from lakes covering the past 10 ka and beyond, for example, Lake Yogo (Hyodo et al., 1993); Beppu Bay (Ohno et al., 1991); Shikoku, Japan Sea (Ohno et al., 1993); Sun-Moon Lake, Taiwan (Lee et al., 2002); Lake Tangra Yumco, Tibetan Plateau (Henkel et al., 2016); MD06-3040, China Sea (Zheng et al., 2014); Mavora Lakes, New Zealand (Turner et al., 2015); LPA and PTA03, Laguna Potrok Aike, Argentina (Gogorza et al., 2012; Kliem et al., 2013; Lisé-Pronovost et al., 2013); and Indonesian records from South Makassar Basin and Celebs Sea (Lund et al., 2006).

### 4.2. Dipole Moment Variations

The temporal variation of the axial dipole moment (ADM) of the GGF100k model is compared with the ADM of CALS10k.2 and virtual axial dipole moment (VADM) reconstructions GLOPIS-75 (Laj et al., 2004), PISO-1500 (Channell et al., 2009), and PADM2 M (Ziegler et al., 2011) in Figure 6. Very long term trends in all reconstructions agree rather well, though the broad maximum at about 50 ka BP appears with different amplitudes. The GGF100k model does not predict values as high as GLOPIS-75 ($13.1 \times 10^{22}$ Am$^2$ at 47 ka BP is the maximum over the stack span) and PISO-1500 ($10.86 \times 10^{22}$ Am$^2$ at 50 ka, which is the maximum for the past 100 ka). This deviation probably results from the combination of GGF100k allowing variability in non–axial dipole variations (unlike the VADM reconstructions) and using a larger number of records not all of which have consistent age control. The presence of low-resolution sediment records that are less easily correlated may damp and smooth the paleomagnetic signal. However, the GGF100k ADM average of $6.78 \times 10^{22}$ Am$^2$ agrees well with the PISO-1500 average over the same time period ($6.81 \times 10^{22}$ Am$^2$) and it is close to the 100-ka average of both PADM2 M ($6.04 \times 10^{22}$ Am$^2$) and GLOPIS ($7.13 \times 10^{22}$ Am$^2$). On the shorter Holocene interval, the mean of GGF100k is comparable to the CALS10k.2 ($8.10 \times 10^{22}$ Am$^2$ and $8.29 \times 10^{22}$ Am$^2$, respectively). A comparison of the actual GGF100k ADM with synthetic predictions from the GGF100k model of the VADM stacks given in GLOPIS-75 and PISO-1500 is presented in supporting information Figure S14. While the synthetic VADM stacks generally resemble the GGF100k ADM variations, slight differences are visible. For example, during the Laschamp excursion the synthetic stack of VADMs reaches slightly lower values, and higher average VADMs appear over the time interval ~45–55 ka BP. In the latter interval both GLOPIS-75 and PISO-1500 VADM stacks are still higher than the GGF100k synthetic stacks. A similar result is seen in comparison to GLOPIS-75 from 30 to 35 ka where large fluctuations are not mirrored in either of the GGF100k results. These rapid variations are not seen in PISO-1500. An ADM of $8.18 \times 10^{22}$ Am$^2$ at 1950 Common Era (0 BP) is consistent with the DGRF value for 1950 of $7.90 \times 10^{22}$ Am$^2$. The ADM variations are also a reflection of global $^{10}$Be production rates (e.g., Frank et al., 1997; Ménabréaz et al., 2012; Simon et al., 2016). The global stack of $^{10}$Be production rate (Frank et al., 1997) suggests an almost constant production rate during the Holocene, increasing rates until the time of the Laschamp excursion (a maximum is reached at 30–42 ka BP), followed by a short period of

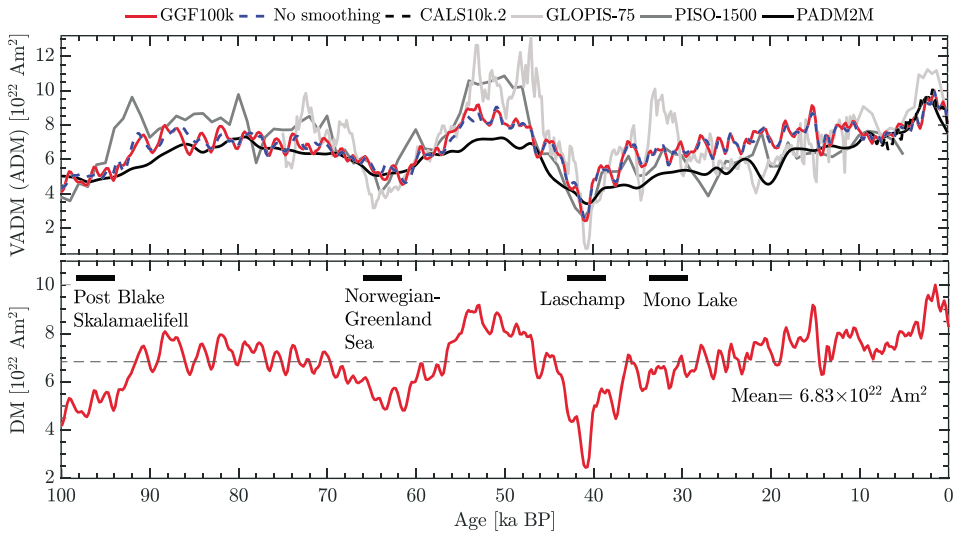


**Figure 6.** (top) Comparison of the axial dipole moment variations of the GGF100k model with available paleomagnetic models and VADM reconstructions from relative paleointensity stacks: CALS10k.2 (Constable et al., 2016); GLOPIS-75 (Laj et al., 2004); PISO-1500 (Channell et al., 2009); and PADM2 M (Ziegler et al., 2011). In addition, a geomagnetic field model with the same damping parameters as for the GGF100k model but no smoothing kernels is plotted with dashed blue line. (bottom) Dipole moment variations of the GGF100k model and the average over the past 100 ka. Times of reported geomagnetic excursions correspond to a dipole moment lower than the mean value. VADM = virtual axial dipole moment.

decreased production rates (45–55 ka BP) and another less pronounced peak from 60 to 75 ka BP. The highest production rate in the 100-ka time interval is always associated with the Laschamp geomagnetic dipole low.

In GGF100k the lowest ADM occurs during the Laschamp excursion at 40.85 ka BP with a value of 2.44 × $10^{22}$ $Am^2$, and the highest value of 9.89 × $10^{22}$ $Am^2$ is predicted at 1.5 ka BP. The GLOPIS-75 VADM value for the Laschamp of 0.8 × $10^{22}$ $Am^2$ at 41.0 ka BP is lower than for the GGF100k, but two aspects have to be considered regarding GLOPIS-75: all 24 RPI records are correlated to a master curve in order to put the records on the same age scale and the final stack is calibrated with the value of the intensity low at 41 ka BP obtained from volcanic outcrops at Laschamp in Central France and in Iceland (Laj et al., 2004). GGF100k is a global model constrained by 135 RPI records that uses no age model adjustments, and calibration to absolute values is performed during the inversion with the help of absolute volcanic and archeomagnetic data. The very low dipole moment in GLOPIS-75 may be exaggerated by the strategy of age alignments, but, even supposing it is accurate, the rapid changes could not be resolved in GGF100k. However, the Laschamp dipole low in GGF100k is comparable with that in PISO-1500 (2.61 × $10^{22}$ $Am^2$) and lower than PADM2 M (3.42 × $10^{22}$ $Am^2$). GGF100k provides better temporal resolution than these two reconstructions. Overall, the GGF100k model predicts a weak dipole moment, notably lower than the average, during three main periods: around the Laschamp event at ~41 ka, at 60–65 ka around the proposed but not so well-documented Norwegian-Greenland Sea excursion, and during the 92- to 100-ka period that encompasses the post-Blake or Skálamælifell excursion (Figure 6). Although the Mono Lake excursion appears to be represented by a rather low value of VADM at ~35 ka in the GLOPIS-75 record, this is not a strong feature in GGF100k. $^{10}$Be-derived geomagnetic dipole moment variations present the weakest values of 1.0 × $10^{22}$ $Am^2$ and 1.4 × $10^{22}$ $Am^2$ during the Laschamp excursion (Ménabréaz et al., 2012; Simon et al., 2016).

### 4.3. Time-Averaged Field

In addition to temporal variations over the past 100 ka, the time-averaged field can also be of interest as an indication of long-term departures of the field from the geocentric axial dipole (GAD). Time averages of radial field component ($B_r$) and non–axial dipole part of $B_r$ at the CMB, as well as the declination and inclination anomaly (difference in inclination of the total field and GAD) at the Earth's surface were obtained from the mean Gauss coefficients over the past 100 ka (Figure 7). Although the axial dipole contribution strongly prevails, a North Atlantic flux lobe dominates $B_r$ in the time-averaged field, in contrast to time-averaged $B_r$ field over the Holocene where two regions of intense normal flux appear in the Northern Hemisphere, over Asia and North America (e.g., see the Holocene models and time-averaged fields in Panovska et al., 2015).

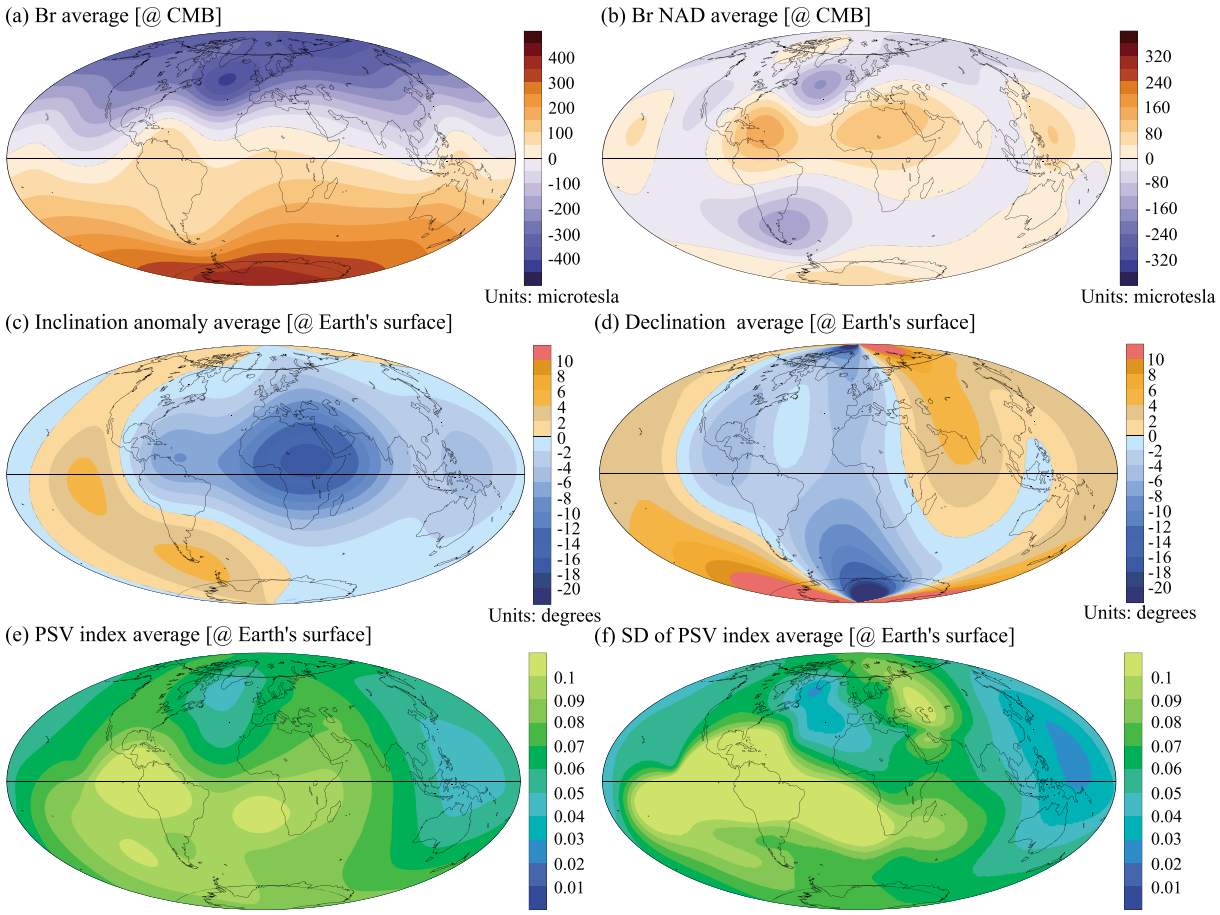


**Figure 7.** Time averages over the past 100 ka from the GGF100k model: (a) radial field component at the CMB; (b) radial component of the non–axial dipole field at the CMB; (c) inclination anomaly at the Earth's surface; (d) declination at the Earth's surface; (e) PSV index and (f) PSV index variability (expressed by the standard deviation, SD). CMB = core-mantle boundary; PSV = paleomagnetic secular variations.

The 100-ka-averaged $B_r$ non–axial dipole field shows positive anomalies over west Atlantic Ocean/Gulf of Mexico, north central Africa, and western equatorial Pacific and two negative anomaly patches with centers in the North and South Atlantic. This structure can mainly be described by axial quadrupole and axial octupole terms (~4% and ~2.5% of the axial dipole, respectively; see supporting information Figures S15 and S16), with the axial quadrupole contribution being recognized as a feature of the geomagnetic field for the past 5 Ma (McElhinny, 2004). Besides these, non–zonal dipole, quadrupole, and octupole contributions persist in the 100-ka average and lead to significant deviation of the geomagnetic field from the GAD. In particular, $g_1^1$ and $h_1^1$ contributions are notably higher compared to the Holocene CALS10k.2 model (supporting information Figure S16).

Both the time-averaged inclination anomaly and declination at the Earth's surface have one large positive and one negative sector. Time-averaged declinations exhibit in general positive values in the Pacific hemisphere and negative in the Atlantic Hemisphere with two centers located near poles where naturally the declination is strongest. The negative inclination anomaly spreads in the equatorial region, with a peak over Africa and smaller peaks in western parts of the Pacific and Atlantic, and it is responsible for the northward bending of the magnetic equator in these regions. The positive inclination anomaly is weaker and covers the Pacific region at all latitudes. Middle to higher latitudes, in general, have smaller inclination anomalies. The inclination anomaly average structure seen in the GGF100k model is similar to those observed in the Holocene models ARCH10k.1, CALS10k.2, and HFM.OL1.A1 (Constable et al., 2016) indicating the longevity of non-GAD field contributions.

To test the hemispheric asymmetry in the time-averaged field and secular variation, we plotted the averages of the PSV index and its variability with time (Panovska & Constable, 2017) in Figure 7. Spatial variations of the averaged index suggest stronger deviations from an axial dipole field in the Southern Hemisphere. South

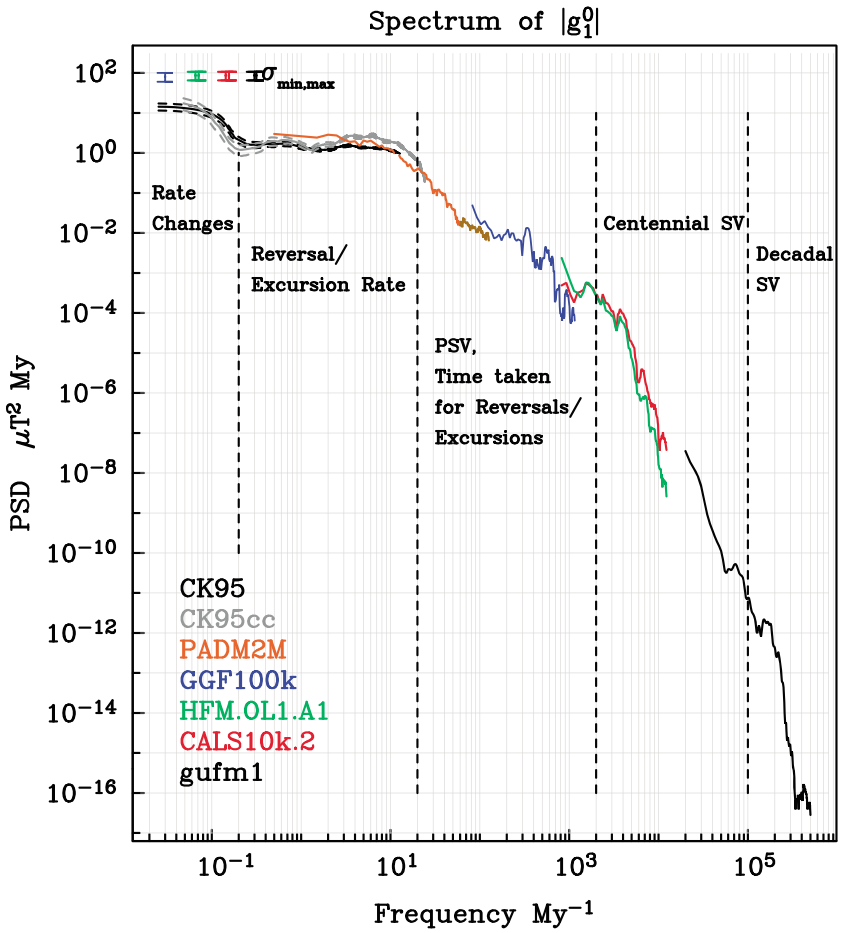


**Figure 8.** Power spectral density (PSD) estimates of the geomagnetic dipole moment constructed from 0- to 160-Ma reversal record (CK95); 0- to 83-Ma reversal record including cryptochrons (CK95cc; Cande & Kent, 1995); 2-Ma paleomagnetic axial dipole moment reconstruction PADM2 M (Ziegler et al., 2011); Holocene geomagnetic field models HFM.OL1.A1 and CALS10k.2 (Constable et al., 2016); the historical geomagnetic field model *gufm1* (Jackson et al., 2000); and the new geomagnetic field model over the past 100 ka—GGF100k.

Atlantic and South America are the regions where the paleomagnetic field over the past 100 ka exhibits more transitional behavior compared to the West Pacific, where the PSV index is very low throughout the whole period. While large patches of high PSV activity cover the South Atlantic, South America, and South East Pacific, the largest part of the Pacific hemisphere is characterized by very low PSV activity. The Laschamp excursion has a notable effect on the PSV activity, and even though it is short in duration, it is the most dramatic event in the past 100 ka. If the excursion is excluded from the estimation of the time averages (supporting information Figure S17), the maximum PSV activity appears on two locations, South Africa/Indian Ocean and South America. However, peak activities still cover larger regions and spread in southern equatorial and midlatitudes, and the Southern hemisphere, in general, exhibits higher paleosecular variation activity confirming the hemispherical asymmetry seen in the Holocene models (Constable et al., 2016). We performed two tests to confirm the robustness of the time average structure by reconstructing the model from synthetic data with very different global distribution. The first model was built from GGF100k model predictions at data locations with Northern and Southern Hemisphere latitudes flipped. The second was built from locations rotated by 180° in longitude; that is, we shifted the Atlantic and Pacific hemisphere locations. Similar structures to GGF100k were resolved with these two models, indicating that the data density does not influence the amount of resolved structure (supporting information Figure S18).

### 4.4. Power Spectrum

One of the goals of building a model over the past 100 ka was to complete the power spectrum of geomagnetic field variations over the full range of frequencies. The spectrum presented in Figure 8 is estimated with

the multitaper spectral estimation technique (Constable & Johnson, 2005). The spectrum estimates of the GGF100k model lie in the frequency range 100–1,000 $Ma^{-1}$ bridging the gap between the centennial secular variation and reversal scales. At lower frequencies, the spectrum agrees with the PADM2 M estimates, while at higher frequencies it fits the Holocene models. CALS10k.2 and HFM.OL1.A1 have more energy at this part of the spectrum because they have higher temporal resolution compared to GGF100k. The slope of the spectrum is similar to those of the Holocene models indicating that the same process may operate on Holocene and 100-ka timescales. High-resolution models covering geomagnetic excursions will refine the spectrum and provide additional information on the geomagnetic field behavior in transitional states.

## 5. Conclusions

We have presented the first global, time-dependent model covering the past 100 ka. The GGF100k model is constrained by more than 100 sediment records and available volcanic and archeomagnetic data. The data distribution resolves comparable spatial power (approximately up to spherical harmonic degree and order 5) but less temporal complexity compared to Holocene geomagnetic field models. Sediment data are treated as time-weighted estimates by smoothing kernels implemented in the forward modeling, which allowed the recovery of higher frequency variations in regions where mixed high- and low-resolution sediment records exist. Although we have employed a Gaussian kernel in this model to describe the smoothing present in the sediment records, the implementation is not limited to this distribution. If, for instance, the postdepositional remanent magnetization is considered, then a different lock-in function (e.g., Mellström et al., 2015; Nilsson et al., 2018) can be used. Axial dipole moment variations show general agreement, but some important differences from the VADM paleointensity stacks GLOPIS-75 and PISO-1500 exist. The lowest dipole moment over the past 100 ka is observed during the Laschamp excursion, $2.46 \times 10^{22}$ $Am^2$ at 40.9 ka BP.

Although the GGF100k model is constrained by a considerable number of data records and many features should be recovered reasonably well, limitations still exist. One of the major drawbacks is associated with the age models and age uncertainties. Discrepancies in ages can distort the global picture and in particular hinder the high-resolution modeling of transitional events. In the future, more high quality data, stricter selection criteria, independent age controls, and updated age models to the latest calibration curves are needed to improve the long-timescale geomagnetic field models. For studies on Holocene timescales, the use of millennial-scale models, such as CALSx and HFM, is recommended because these models have higher temporal resolution and better defined robust features (Constable et al., 2016; Korte et al., 2011; Panovska et al., 2015). The GGF100k model provides more detailed information on changes in the structure of the geomagnetic field which are related to changes in the production rate of cosmogenic isotopes over the past 100 ka.

**Acknowledgments**
This work has been supported under NSF grants EAR 1246826 and EAR 1623786. S. P. gratefully acknowledges support from the Swiss National Science Foundation grant PBEZP2-142912. C. G. C. thanks GFZ Potsdam and the Alexander von Humboldt Foundation for their remarkable hospitality and generous support of repeated research visits over a number of years. We also thank Gillian Turner and an anonymous reviewer for their constructive comments and suggestions. The GGF100k model coefficients and its 100-ka time average are available from the EarthRef Digital Archive under the link https://earthref.org/ERDA/2382/ and in the supporting information for this article.

## References

Baumgartner, S., Beer, J., Masarik, J., Wagner, G., Meynadier, L., & Synal, H.-A. (1998). Geomagnetic modulation of the $^{36}Cl$ flux in the GRIP Ice Core Greenland. *Science*, *279*(5355), 1330–1332.

Bloxham, J., & Jackson, A. (1992). Time-dependent mapping of the magnetic field at the core-mantle boundary. *Journal of Geophysical Research*, *97*, 19,537–19,563.

Bourne, M. D., Mac Niocaill, C., Thomas, A. L., & Henderson, G. M. (2013). High-resolution record of the Laschamp geomagnetic excursion at the Blake-Bahama Outer Ridge. *Geophysical Journal International*, *195*, 1519–1533.

Brown, M. C., Donadini, F., Korte, M., Nilsson, A., Korhonen, K., Lodge, A., et al. (2015). GEOMAGIA50.v3: 1. General structure and modifications to the archeological and volcanic database. *Earth Planets Space*, *67*, 83.

Brown, M. C., Donadini, F., Nilsson, A., Panovska, S., Frank, U., Korhonen, K., et al. (2015). GEOMAGIA50.v3: 2. A new paleomagnetic database for lake and marine sediments. *Earth Planets Space*, *67*, 70.

Brown, M. C., Korte, M., Holme, R., Wardinski, I., & Gunnarson, S. (2018). Earth's magnetic field is probably not reversing. *Proceedings of the National Academy of Sciences of the United States of America*, *115*(20), 5111–5116.

Cande, S. C., & Kent, D. V. (1995). Revised calibration of the geomagnetic polarity timescale for the Late Cretaceous and Cenozoic. *Journal of Geophysical Research*, *100*, 6093–6095.

Channell, J. E. T. (1999). Geomagnetic paleointensity and directional secular variation at Ocean Drilling Program (ODP) Site 984 (Bjorn Drift) since 500 ka: Comparisons with ODP Site 983 (Gardar Drift). *Journal of Geophysical Research*, *104*(B10), 22,937–22,951.

Channell, J. E. T., Harrison, R. J., Lascu, I., McCave, I. N., Hibbert, F. D., & Austin, W. E. N. (2016). Magnetic record of deglaciation using FORC-PCA, sortable-silt grain size, and magnetic excursion at 26 ka, from the Rockall Trough (NE Atlantic). *Geochemistry, Geophysics, Geosystems*, *17*, 1823–1841. https://doi.org/10.1002/2016GC006300

Channell, J. E. T., Hodell, D. A., & Lehman, B. (1997). Relative geomagnetic paleointensity and $\delta^{18}O$ at ODP Site 983 (Gardar Drift, North Atlantic) since 350 ka. *Earth and Planetary Science Letters*, *153*, 103–118.

Channell, J. E. T., Stoner, J. S., Hodell, D., & Charles, C. D. (2000). Geomagnetic paleointensity for the last 100 kyr from the sub-antarctic South Atlantic: A tool for inter-hemispheric correlation. *Earth and Planetary Science Letters*, *175*, 145–160.

Channell, J. E. T., Xuan, C., & Hodell, D. A. (2009). Stacking paleointensity and oxygen isotope data for the last 1.5 Myr (PISO-1500). *Earth and Planetary Science Letters*, *283*, 14–23.

Constable, C. G., & Johnson, C. L. (2005). A paleomagnetic power spectrum. *Physics of the Earth and Planetary Interiors*, *153*, 61–73.
Constable, C. G., Koppers, A. A., Tauxe, L., & Minnett, R. (2006). The five dimensions of MagIC. Fall Meeting, AGU, San Francisco Abstract IN13C–1172.
Constable, C. G., Korte, M., & Panovska, S. (2016). Persistent high paleosecular variation activity in Southern Hemisphere for at least 10 000 years. *Earth and Planetary Science Letters*, *453*, 78–86.
Constable, C. G., & Parker, R. L. (1988). Smoothing, splines and smoothing splines; their application in geomagnetism. *Journal of Computational Physics*, *78*, 493–508.
Cromwell, G., Johnson, C. L., Tauxe, L., Constable, C. G., & Jarboe, N. (2018). PSV10: A global data set for 0–10 Ma time-averaged field and paleosecular variation studies. *Geochemistry, Geophysics, Geosystems*, *19*. https://doi.org/10.1002/2017GC007318
De Boor, C. (2001). *A practical guide to splines*. New York: Springer.
Diepenbroek, M., Grobe, H., Reinke, M., Schindler, U., Schlitzer, R., Sieger, R., & Wefer, G. (2002). PANGAEA—An information system for environmental sciences. *Computers & Geosciences*, *28*, 1201–1210.
Donadini, F., Korte, M., & Constable, C. G. (2009). Geomagnetic field for 0–3 ka: 1. New data sets for global modelling. *Geochemistry, Geophysics, Geosystems*, *10*, Q06007. https://doi.org/10.1029/2008GC002295
Finlay, C. C., Aubert, J., & Gillet, N. (2016). Gyre-driven decay of the Earth's magnetic dipole. *Nature Communications*, *7*, 10422.
Finlay, C. C., Jackson, A., Gillet, N., & Olsen, N. (2012). Core surface magnetic field evolution 2000–2010. *Geophysical Journal International*, *189*, 761–781.
Frank, M., Schwarz, B., Baumann, S., Kubik, P. W., Suter, M., & Mangini, A. (1997). A 200 kyr record of cosmogenic radionuclide production rate and geomagnetic field intensity from $^{10}$Be in globally stacked deep-sea sediments. *Earth and Planetary Science Letters*, *149*, 121–129.
Gogorza, C. S. G., Irurzun, M. A., Sinito, A. M., Lisé-Pronovost, A., St-Onge, G., Haberzettl, T., et al. (2012). High-resolution paleomagnetic records from Laguna Potrok Aike (Patagonia, Argentina) for the last 16,000 years. *Geochemistry, Geophysics, Geosystems*, *13*, Q12Z37. https://doi.org/10.1029/2011GC003900
Gubbins, D. (1987). Mechanism for geomagnetic polarity reversals. *Nature*, *326*, 167–169.
Gubbins, D., & Bloxham, J. (1985). Geomagnetic field analysis—III. Magnetic fields on the core-mantle boundary. *Geophysical Journal of the Royal Astronomical Society*, *80*, 695–713.
Gubbins, D., & Kelly, P. (1993). Persistent patterns in the geomagnetic field over the past 2.5 Myr. *Nature*, *365*, 829–832.
Guyodo, Y., & Valet, J.-P. (1996). Relative variations in geomagnetic intensity from sedimentary records: The past 200,000 years. *Earth Planetary Science Letters*, *143*, 23–36.
Guyodo, Y., & Valet, J.-P. (1999). Global changes in intensity of the Earth's magnetic field during the past 800 kyr. *Nature*, *399*, 249–252.
Hayashida, A., Ali, M., Kuniko, Y., Kitagawa, H., Torii, M., & Takemura, K. (2007). Environmental magnetic record and paleosecular variation data for the last 40 kyrs from the Lake Biwa sediments, Central Japan. *Earth Planets and Space*, *59*, 807–814.
Henkel, K., Haberzettl, T., St-Onge, G., Wang, J., Ahlborn, M., Daut, G., et al. (2016). High-resolution paleomagnetic and sedimentological investigations on the Tibetan Plateau for the past 16 ka cal B.P.- The Tangra Yumco record. *Geochemistry, Geophysics, Geosystems*, *17*, 774–790. https://doi.org/10.1002/2015GC006023
Hulot, G., Eymin, C., Langlais, B., Mandea, M., & Olsen, N. (2002). Small-scale structure of the geodynamo inferred from Oersted and Magsat satellite data. *Nature*, *416*, 620–623.
Hyodo, M., Itota, C., & Yaskawa, K. (1993). Geomagnetic secular variation reconstructed from magnetizations of wide-diameter cores of Holocene sediments in Japan. *Journal of Geomagnetism and Geoelectricity*, *45*, 669–969.
Jackson, A., Jonkers, A. R. T., & Walker, M. R. (2000). Four centuries of geomagnetic secular variation from historical records. *Philosophical Transactions of the Royal Society of London A*, *358*, 957–990.
Jarboe, N. A., Koppers, A. A., Tauxe, L., Minnett, R., & Constable, C. G (2012). The online MagIC database: Data archiving, compilation, and visualization for the geomagnetic, paleomagnetic and rock magnetic communities. Fall Meeting, AGU, San Francisco. Abstract GP31A-1063.
Jicha, B. R., Kristjánsson, L., Brown, M. C., Singer, B. S., Beard, B. L., & Johnson, C. M. (2011). New age for the Skálamælifell excursion and identification of a global geomagnetic event in the late Brunhes chron. *Earth and Planetary Science Letters*, *310*, 509–517.
Johnson, C. L., & Constable, C. G. (1995). The time-averaged geomagnetic field as recorded by lava flows over the past 5 Myr. *Geophysical Journal International*, *122*, 489–519.
Johnson, C. L., & Constable, C. G. (1997). The time-averaged geomagnetic field: Global and regional biases for 0–5 Ma. *Geophysical Journal International*, *131*, 643–666.
Kelly, P., & Gubbins, D. (1997). The geomagnetic field over the past 5 million years. *Geophysical Journal International*, *128*, 315–330.
Kliem, P., Enters, D., Hahn, A., Ohlendorf, C., Lisé-Pronovost, A., St-Onge, G., et al. (2013). And the PASADO science team. Lithology, radiocarbon dating and sedimentological interpretation of the 51 ka BP lacustrine record from Laguna Potrok Aike, southern Patagonia. *Quaternary Science Reviews*, *71*, 54–69.
Korhonen, K., Donadini, F., Riisager, P., & Pesonen, L. J. (2008). Geomagia50: An archeointensity database with PHP and MySQL. *Geochemistry, Geophysics, Geosystems*, *9*, Q04029. https://doi.org/10.1029/2007GC001893
Korte, M., & Constable, C. G. (2003). Continuous global geomagnetic field models for the past 3000 years. *Physics of the Earth and Planetary Interiors*, *140*, 73–89.
Korte, M., & Constable, C. G (2005). Continuous geomagnetic field models for the past 7 millennia: 2. CALS7K. *Geochemistry, Geophysics, Geosystems*, *6*, Q02H16. https://doi.org/10.1029/2004GC000800
Korte, M., & Constable, C. G. (2008). Spatial and temporal resolution of millennial scale geomagnetic field models. *Advances in Space Research*, *41*, 57–69.
Korte, M., & Constable, C. G. (2011). Improving geomagnetic field reconstructions for 0–3 ka. *Physics of the Earth and Planetary Interiors*, *188*, 247–259.
Korte, M., Constable, C. G., Donadini, F., & Holme, R. (2011). Reconstructing the Holocene geomagnetic field. *Earth and Planetary Science Letters*, *312*, 497–505.
Korte, M., Donadini, F., & Constable, C. G. (2009). Geomagnetic field for 0–3 ka: 2. A new series of time-varying global models. *Geochemistry, Geophysics, Geosystems*, *10*, Q06008. https://doi.org/10.1029/2008GC002297
Laj, C., & Channell, J. E. T. (2015). 5.10 Geomagnetic excursions. In G. Schubert (Ed.), *Treatise on geophysics* (Vol. 5, 2nd ed., pp. 343–383). Amsterdam: Elsevier.
Laj, C., & Kissel, C. (2015). An impending geomagnetic transition? Hints from the past. *Frontiers in Earth Science*, *3*, 61.
Laj, C., Kissel, C., & Beer, J. (2004). High resolution global paleointensity stack since 75 kyr (GLOPIS-75) calibrated to absolute values (Vol. 145). In J. E. T. Channell et al. (Eds.), *In Channell, J.E.T. Timescales of the paleomagnetic field, Geophysical Monograph* (pp. 255–265). Washington, DC: AGU.

Laj, C., Kissel, C., & Roberts, A. P. (2006). Geomagnetic field behavior during the Iceland Basin and Laschamp geomagnetic excursions: A simple transitional field geometry? *Geochemistry, Geophysics, Geosystems*, *7*, Q03004. https://doi.org/10.1029/2005GC001122

Lee, T.-Q., Lou, W.-C., & Liew, P.-M. (2002). Paleomagnetic study of lacustrine sediments from Sun-Moon Lake, central Taiwan. *West Pac Earth Science*, *2*(1), 15–26.

Leonhardt, R., Fabian, K., Winklhofer, M., Ferk, A., Laj, C., & Kissel, C. (2009). Geomagnetic field evolution during the Laschamp excursion. *Earth and Planetary Science Letters*, *278*, 87–95.

Lisé-Pronovost, A., St-Onge, G., Gogorza, C. S. G., Haberzettl, T., Preda, M., Kliem, P., et al. (2013). The PASADO Science Team. High-resolution paleomagnetic secular variations and relative paleointensity since the Late Pleistocene in southern South America. *Quaternary Science Reviews*, *71*, 91–108.

Lund, S. P., Schwartz, M., Keigwin, L., & Johnson, T. (2005). Deep-sea sediment records of the Laschamp geomagnetic field excursion (~41,000 calender years before present). *Journal of Geophysical Research*, *110*, B04101. https://doi.org/10.1029/2003JB002943

Lund, S. P., Stott, L., Schwartz, M., Thunell, R., & Chen, A. (2006). Holocene paleomagnetic secular variation records from the western equatorial Pacific Ocean. *Earth and Planetary Science Letters*, *246*, 381–392.

McElhinny, M. W. (2004). Geocentric axial dipole hypothesis: A least squares perspective (Vol. 145). In J. E. T. Channell et al. (Eds.), *In Channell, J. E. T. Timescales of the paleomagnetic field* (pp. 1–12).: AGU Geophysical Monograph.

Mellström, A., Nilsson, A., Stanton, T., Muscheler, R., Snowball, I., & Suttie, N. (2015). Post-depositional remanent magnetization lock-in depth in precisely dated varved sediments assessed by archaeomagnetic field models. *Earth and Planetary Science Letters*, *410*, 186–196.

Ménabréaz, L., Bourlès, D. L., & Thouveny, N. (2012). Amplitude and timing of the Laschamp geomagnetic dipole low from the global atmospheric $^{10}$Be overproduction: Contribution of authigenic $^{10}$Be/$^{9}$Be ratios in west equatorial Pacific sediments. *Journal of Geophysical Research*, *117*, B11101. https://doi.org/10.1029/2012JB009256

Nilsson, A., Holme, R., Korte, M., Suttie, N., & Hill, M. (2014). Reconstructing Holocene geomagnetic field variation: New methods, models and implications. *Geophysical Journal International*, *198*(1), 229–248.

Nilsson, A., Suttie, N., & Hill, M. J. (2018). Short-term magnetic field variations from the post-depositional remanence of lake sediments. *Frontiers in Earth Science*, *6*, 39. https://doi.org/10.3389/feart.2018.00039

Nowaczyk, N. R., Frank, U., Kind, J., & Arz, H. W. (2013). A high-resolution paleointensity stack of the past 14 to 68 ka from Black Sea sediments. *Earth and Planetary Science Letters*, *384*, 1–16.

Nowaczyk, N. R., Frederichs, T. W., Eisenhauer, A., & Gard, G. (1994). Magnetostratigraphic data from late Quaternary sediments from the Yermak Plateau, Arctic Ocean Evidence for four geomagnetic polarity events within the last 170 ka of the Brunhes Chron. *Geophysical Journal International*, *117*, 453–471.

Ohno, M., Hamano, Y., Murayama, M., Matsumoto, E., Iwakura, H., Nakamura, T., & Taira, A. (1993). Paleomagnetic record over the past 35,000 years of a sediment core from off Shikoku, southwest Japan. *Geophysical Research Letters*, *20*(13), 1395–1398.

Ohno, M., Hamano, Y., Okamura, M., & Shimazaki, K. (1991). Geomagnetic secular variation curve in the sediment from Beppu Bay, Kyushu, Japan Rock Ma. *Paleogeophys*, *18*, 68–74.

Olsen, N., Hulot, G., Lesur, V., Finlay, C. C., Beggan, C., Chulliat, A., et al. (2015). The Swarm Initial Field Model for the 2014 geomagnetic field. *Geophysical Research Letters*, *42*, 1092–1098. https://doi.org/10.1002/2014GL062659

Panovska, S., & Constable, C. G. (2017). An activity index for geomagnetic paleosecular variation, excursions, and reversals. *Geochemistry, Geophysics, Geosystems*, *18*, 1366–1375. https://doi.org/10.1002/2016GC006668

Panovska, S., Constable, C. G., & Brown, M. C. (2018). Global and regional assessments of paleosecular variation activity over the past 100 ka. *Geochemistry, Geophysics, Geosystems*, *19*. https://doi.org/10.1029/2017GC007271

Panovska, S., Finlay, C. C., Donadini, F., & Hirt, A. M. (2012). Spline analysis of Holocene sediment magnetic records: Uncertainty estimates for field modelling. *Journal of Geophysical Research*, *117*, B02101. https://doi.org/10.1029/2011JB008813

Panovska, S., Korte, M., Finlay, C. C., & Constable, C. G. (2015). Limitations in paleomagnetic data and modelling techniques and their impact on Holocene geomagnetic field models. *Geophysical Journal International*, *202*, 402–418.

Parker, R. L. (1994). *Theory, geophysical inverse*. Princeton: Princeton University Press.

Pavón-Carrasco, F. J., & De Santis, A. (2016). The South Atlantic Anomaly: The key for a possible geomagnetic reversal. *Frontiers in Earth Science*, *4*, 40.

Pavón-Carrasco, F. J., Osete, M. L., Torta, J. M., & De Santis, A. (2014). A geomagnetic field model for the Holocene based on archaeomagnetic and lava flow data. *Earth and Planetary Science Letters*, *388*, 98–109.

Roberts, A. P. (2008). Geomagnetic excursions: Knowns and unknowns. *Geophysical Research Letters*, *35*, L17307. https://doi.org/10.1029/2008GL034719

Simon, Q., Thouveny, N., Bourlès, D. L., Valet, J.-P., Bassinot, F., Ménabréaz, L., et al. (2016). Authigenic $^{10}$Be/$^{9}$Be ratio signatures of the cosmogenic nuclide production linked to geomagnetic dipole moment variation since the Brunhes/Matuyama boundary. https://doi.org/10.1002/2016jb013335

Singer, B. S. (2014). A Quaternary geomagnetic instability time scale. *Quaternary Geochronology*, *21*, 29–52.

Singer, B. S., Jicha, B. R., He, H., & Zhu, R. (2014). Geomagnetic field excursion recorded 17 ka at Tianchi Volcano, China: New $^{40}$Ar/$^{39}$Ar age and significance. *Geophysical Research Letters*, *41*, 2794–2802. https://doi.org/10.1002/2014GL059439

Stoner, J. S., Channell, J. E. T., Hillaire-Marcel, C., & Kissel, C. (2000). Geomagnetic paleointensity and environmental record from Labrador Sea core MD95-2024: Global marine sediment and ice core chronostratigraphy for the last 110 kyr. *Earth and Planetary Science Letters*, *183*, 161–177.

Stoner, J. S., Channell, J. E. T., Hodell, D. A., & Charles, C. D. (2003). A ~580 kyr paleomagnetic record from the sub-Antarctic South Atlantic (Ocean Drilling Program Site 1089). *Journal of Geophysical Research*, *108*(B5), 2244.

Stoner, J. S., Laj, C., Channell, J. E. T., & Kissel, C. (2002). South Atlantic and North Atlantic geomagnetic paleointensity stacks (0–80 ka): Implications for inter-hemispheric correlation. *Quaternary Science Reviews*, *21*, 1141–1151.

Tauxe, L., & Yamazaki, T. (2007). Paleointensities. In G. Schubert (Ed.), *Treatise of geophysics, geomagnetism* (pp. 509–563). Amsterdam: Elsevier. https://doi.org/10.1016/B978-044452748-6.00098-5

Thouveny, N., Carcaillet, J., Moreno, E., Leduc, G., & Nérini, D. (2004). Geomagnetic moment variation and paleomagnetic excursions since 400 kyr BP: A stacked record from sedimentary sequences of the Portuguese margin. *Earth and Planetary Science Letters*, *219*, 377–396.

Thouveny, N., Creer, K. M., & Blunk, I. (1990). Extension of the Lac du Bouchet palaeomagnetic record over the last 120,000 years. *Earth and Planetary Science Letters*, *97*, 140–161.

Turner, G. M., Howarth, J. D., de Gelder, G. I. N. O., & Fitzsimons, S. J. (2015). A new high-resolution record of Holocene geomagnetic secular variation from New Zealand. *Earth and Planetary Science Letters*, *430*, 296–307.

Valet, J.-P., Meynadier, L., & Guyodo, Y. (2005). Geomagnetic dipole strength and reversal rate over the past two million years. *Nature*, *435*, 802–805.

Worm, H.-U. (1997). A link between geomagnetic reversals and events and glaciations. *Earth and Planetary Science Letters*, *147*, 55–67.
Yamazaki, T. (1999). Relative paleointensity of the geomagnetic field during Brunhes Chron recorded in North Pacific deep-sea sediment cores: Orbital influence. *Earth and Planetary Science Letters*, *169*, 23–35.
Yamazaki, T., Ioka, N., & Eguchi, N. (1995). Relative paleointensity of the geomagnetic field during the Brunhes Chron. *Earth and Planetary Science Letters*, *136*, 525–540.
Zheng, Y., Zheng, H., Deng, C., & Liu, Q. (2014). Holocene paleomagnetic secular variation from East China Sea and a PSV stack of East Asia. *Physics of the Earth and Planetary Interiors*, *236*, 69–78.
Ziegler, L. B., Constable, C. G., Johnson, C. L., & Tauxe, L. (2011). PADM2M: A penalized maximum likelihood model of the 0–2 Ma palaeomagnetic axial dipole moment. *Geophysical Journal International*, *184*, 1069–1089.